Journal of the Energy Institute 103 (2022) 138–146

Contents lists available at ScienceDirect

Journal of the Energy Institute

journal homepage: www.elsevier.com/locate/joei

Plasma-enhanced catalytic oxidation of ethylene oxide over Fe–Mn based ternary catalysts

Xinbo Zhu [a,*], Haiping Xiong [a], Jin Liu [a], Yuting Gan [a], Zitan Xu [a], Chunlin Zhou [a], Yaolin Wang [b], Ye Jiang [c], Xin Tu [b,*]

[a] Faculty of Maritime and Transportation, Ningbo University, Ningbo, 315211, China
[b] Department of Electrical Engineering and Electronics, University of Liverpool, Liverpool, L69 3GJ, United Kingdom
[c] College of New Energy, China University of Petroleum (East China), Qingdao, 266580, China

ARTICLE INFO

Keywords:
Non-thermal plasma
Plasma catalysis
Volatile organic compound
Ethylene oxide
Fe–Mn based catalysts
Advanced oxidation

ABSTRACT

In this work, Fe–Mn based ternary catalysts (Fe–Mn-X, X = Ce, Co and Cu) were evaluated in the plasma-catalytic oxidation of ethylene oxide (EO) using a cylindrical dielectric barrier discharge (DBD) reactor. The addition of transition metal dopants to the Fe–Mn catalyst significantly improved the performance of plasma-catalyzed EO oxidation compared to the reaction using plasma only and the Fe–Mn catalyst. The highest EO conversion (91.9%) and CO_2 selectivity (78.9%) were obtained over the Fe–Mn–Co catalyst at a specific energy input (SEI) of 730.2 J l^{-1}. Moreover, the presence of water vapor improved EO conversion and CO_2 selectivity in the relative humidity (RH) range of 0–60%, while further increasing the RH to 80% reduced EO conversion. The interactions between Fe, Mn and dopants increased the specific surface area and pore volume of the Fe–Mn-X catalyst, while maintaining the crystalline structure of the catalysts. The presence of the dopants enhanced the reducibility of the Fe–Mn-X catalysts and produced more surface adsorbed oxygen (O_{ads}) on the catalyst surfaces. Moreover, the interactive effects among the Fe, Mn and dopants facilitated the plasma-catalytic oxidation reactions via enhanced surface reactions. The coupling of plasma with the Fe–Mn–Co catalyst reduced the formation of organic by-products in the plasma-catalyzed oxidation of EO.

1. Introduction

Since volatile organic compound (VOC) emissions in waste gas streams from industrial processes and transportation cause serious environmental and health problems, various VOC control technologies have been developed to meet the stringent air quality standards [1–3]. During the past decades, the combination of non-thermal plasma (NTP) technology and heterogeneous catalysis, known as "plasma catalysis", has been regarded as a promising alternative for the purification of waste gas streams with high volume and low VOC concentration [4,5]. The hybrid plasma-catalytic technology is distinguished by features such as relatively high removal efficiency, improved process selectivity, rapid response, system compactness and mild operating conditions [6–8]. NTPs produce a variety of chemically reactive species including energetic electrons, radicals, and excited species, all of which can react with pollutants in the gas phase and on catalyst surfaces [9,10]. In a typical plasma-catalytic system, the interactions between plasma and heterogeneous catalysts have great potential to generate synergistic effects [11,12]. In addition, the coupling of plasma with appropriate catalysts can provide impressive selectivity for the deep oxidation of VOCs and reaction intermediates to final products such as CO_2 and H_2O.

The catalyst composition is critical in determining the performance of plasma-catalytic oxidation of VOCs in terms of conversion, CO_2 selectivity and by-product formation [13,14]. Norsic et al. investigated the effect of γ-Al_2O_3 supported Cu, Mn and Ce catalysts on the plasma-catalytic oxidation of 150 ppm methanol. Among these catalysts, packing Cu/γ-Al_2O_3 into the plasma reactor showed the highest conversion of 74% and CO_x selectivity of ~80% at a specific energy input (SEI) of 20 J l^{-1} [15]. Liu et al. found that the combination of dielectric barrier discharge (DBD) and MnO_x/γ-Al_2O_3 achieved a chlorobenzene conversion of 96.3% and CO_x selectivity of 53.0% at an SEI of 1350 J l^{-1} [16]. The use of mixed metal oxides has been demonstrated to be effective for catalytic oxidation of VOCs. A screening study reported that doping the Co element in the B-site of a perovskite $LaMO_3$ catalyst enhanced ethyl acetate conversion by 20% compared to the reaction using plasma only, while using $LaMnO_3$ and $LaFeO_3$ only enhanced ethyl

* Corresponding author.
E-mail addresses: zhuxinbo@nbu.edu.cn (X. Zhu), xin.tu@liverpool.ac.uk (X. Tu).

https://doi.org/10.1016/j.joei.2022.06.002
Received 24 March 2022; Received in revised form 3 June 2022; Accepted 7 June 2022
Available online 11 June 2022

acetate conversion by 16% and 12%, respectively [17]. Jiang et al. also disclosed that the combination of plasma and CoO_x-CeO_2 enhanced the conversion of 300 ppm toluene by 5%–20% alongside the enhanced CO_2 selectivity by 3%–18%, when compared to the same plasma reaction using single metal oxide catalysts [18]. More recently, Fe–Mn based catalysts have been widely investigated in thermal catalytic oxidation of VOCs, selective catalytic reduction (SCR) of NO_x and fuel refining due to their high catalytic activity, good thermal stability, low cost, and abundant supply of raw material [19–21]. In the aspects of plasma catalysis, Chang et al. investigated formaldehyde oxidation over Fe–Mn oxides in a plasma-catalytic system. The best formaldehyde conversion (95.0%) and CO_2 selectivity (86.2%) were attained over a $Fe_{0.71}Mn$ catalyst at a discharge power of 5 W and a flow rate of 0.5 l min^{-1} [22]. Qi et al. investigated toluene removal using a Fe–Mn/γ-Al_2O_3 catalyst in a NTP-catalysis reactor, obtaining the highest removal efficiency (98.6%) and CO_2 selectivity (88.0%) over Fe1Mn1/γ-Al_2O_3 at an SEI of 1500 J l^{-1} [23]. Tang et al. found that the combination of DBD and granular activated carbon (GAC) supported Fe-Mn performed better in oxytetracycline removal than DBD alone or DBD + virgin GAC [24]. Recently, we reported on the oxidation of ethylene oxide (EO) in a plasma-catalytic system using Fe–Mn catalysts. At an SEI of 656.1 J l^{-1}, the presence of the Fe_1Mn_1 catalyst resulted in the highest EO conversion of 98.8%. However, unfavorable by-products such as CH_3COOH, CH_3CHO and hydrocarbons were detected in this process, suggesting that the formation of by-products in the plasma-catalytic process requires further investigation [25].

Plasma coupling with ternary mixed oxides has the potential to improve the performance of VOC oxidation under plasma conditions even further. Parvizi et al. reported that the incorporation of Co, Zn, Mg and Ba on the A-site of $LaMnO_3$ perovskite-type catalysts significantly improved the performance of BTX (benzene, toluene and xylene) oxidation in a DBD plasma reactor, while the activities of the catalysts followed the order $LaZnMnO_3 > LaMgMnO_3 > LaBaMnO_3 > LaCoMnO_3$. Moreover, the increased CO_2 selectivity during the plasma-catalytic oxidation of BTX confirmed the reduced by-product formation in this process [26]. However, to the best of our knowledge, there is no report on the investigation of plasma-catalytic oxidation of VOCs over ternary Fe–Mn-X mixed oxide catalysts, particularly with regard to the improvement of reaction performance in terms of VOC conversion, CO_2 selectivity and by-products distribution.

Herein, we synthesized Fe–Mn-X (X = Ce, Co and Cu) ternary mixed oxides using the citric acid method. Ethylene oxide was chosen as a model VOC pollutant since it is widely used as a raw material in the chemical industry for the production of germicide, plasticizer and surfactants [27]. The effect of Fe–Mn-X catalysts on the plasma-catalytic oxidation of EO was investigated in terms of EO conversion and CO_2 selectivity. Catalyst characterizations were used to understand the structural properties, crystalline characteristics, surface chemical states, and redox properties of the catalysts. The enhancement of EO oxidation over the Fe–Mn-X catalysts was discussed in terms of reaction performance, by-product formation and catalyst properties.

2. Materials and methods

2.1. Catalyst preparation

In this work, Fe–Mn-X catalysts (X = Ce, Co and Cu) were synthesized using the citric acid method. All of the chemicals were of analytical grade and came from Aladdin Co. Ltd. Firstly, the desired amount of metal nitrates and citric acid were mixed and dissolved in deionized water in a beaker. The obtained solutions had a metal element concentration of 0.1 mol l^{-1}. The molar ratio of citric acid to all metal cations was controlled at 1.5. The obtained solution was magnetically stirred for 1 h at room temperature before standing for another 1 h. The solution was then treated in an 80 °C water bath to produce the viscous wet gel. The wet gels were heated in an oven at 110 °C for 12 h before being calcined at 500 °C for 5 h. For catalyst calcination, the temperature was raised from room temperature to 500 °C at a heating rate of 5 °C min^{-1}. The prepared Fe–Mn-X catalysts are denoted as Fe–Mn–Ce, Fe–Mn–Co and Fe–Mn–Cu, respectively. The third doping element had a relative metal molar concentration of 10%, while the Fe and Mn elements each accounted for 45% of the total metal cations. Moreover, for comparison, Fe–Mn mixed oxide with a Fe/Mn molar ratio of 1:1 was prepared using the same method. All prepared catalysts were sieved in 40–60 meshes before the plasma-catalytic EO oxidation.

2.2. Catalyst characterizations

The N_2 adsorption-desorption experiments were carried out at 77 K using a Quanta Chrome Autosorb-1 instrument. Before each test, the catalysts were degassed for 3 h at 250 °C to remove impurities. The Brunauer-Emmett-Teller (BET) equation was used to calculate the specific surface area (S_{BET}) in the partial pressure range (p/p_0) between 0.05 and 0.35.

The X-ray diffraction (XRD) patterns of the Fe–Mn-X catalysts were recorded using a Rikagu D/max-2000 X-ray diffractometer with Cu-Kα radiation. The scanning range was 10°–80° with a scanning step size of 0.02°.

X-ray photoelectron spectroscopy (XPS) analysis of the catalysts was performed on a Thermo ESCALAB 250 instrument equipped with an Al Kα X-ray source ($h\nu$ = 1486.6 eV). The XPS spectra were calibrated using the C 1s spectra at a binding energy value of 284.6 eV.

The redox properties of the catalysts were analyzed using temperature-programmed reduction of H_2 (H_2-TPR). To remove impurities, 100 mg of catalysts were heated at 250 °C in a helium gas stream for 1 h in each test. After that, the sample was cooled to room temperature. The carrier gas was changed to a 5 vol% H_2/Ar mixture with a flow rate of 30 ml min^{-1}. The temperature was then raised from room temperature to 800 °C at a constant rate of 10 °C min^{-1}. The amount of H_2 consumption was calculated based on the H_2-TPR profiles.

2.3. Plasma-catalytic system

Fig. 1 shows the schematic diagram of the experimental system. A typical coaxial DBD reactor was developed for this reaction. The DBD reactor consists of a quartz tube with an outer diameter of 10 mm and a wall thickness of 8 mm. A stainless-steel rod was placed on the axis of the quartz tube as a high voltage electrode and held by two PTFE seals. The high voltage electrode had a diameter of 4 mm. A 30 mm-long stainless-steel mesh was wrapped around the quartz tube as a ground electrode. The DBD reactor was connected to an AC high voltage power supply (CTP-2000K, Nanjing Suman, China). A measuring capacitor (C_{ext}, 0.47 μF) was placed between the stainless-steel mesh (ground electrode) and the ground. A Testec (HVP–15HF, 1000:1) high voltage probe and a Tektronix P5100 probe were used to measure the applied voltage and voltage across the external capacitor, respectively. Both voltage signals were monitored using a Tektronix 2024D (Tektronix, USA) oscilloscope. The discharge power of the plasma process was calculated using the standard *Q-U* Lissajous method. The discharge power can be controlled by varying the applied voltage across the plasma reactor.

The carrier gas was 21 vol% O_2 (>99.999%) balanced with N_2 (>99.999%) and controlled by mass flow controllers (Sevenstars D07-B, Beijing, China), while EO was generated from a calibrated gas cylinder (0.1 vol% with balanced N_2). Before the reaction, the three gas streams were pre-mixed, and the total gas flow rate was fixed at 1.5 l min^{-1}. When necessary, water vapor was introduced to the DBD reactor by passing a nitrogen flow through a water bubbler kept in an ice-water bath (0 °C), whereas the other gas streams were introduced directly into the mixer. In this work, the relative humidity was controlled between 0 and 80% by passing gas flows through the bubbler at different flow rates. Unless otherwise specified, the EO concentration in this study was kept at 300 ppm. For each test, 100 mg of the catalyst were packed

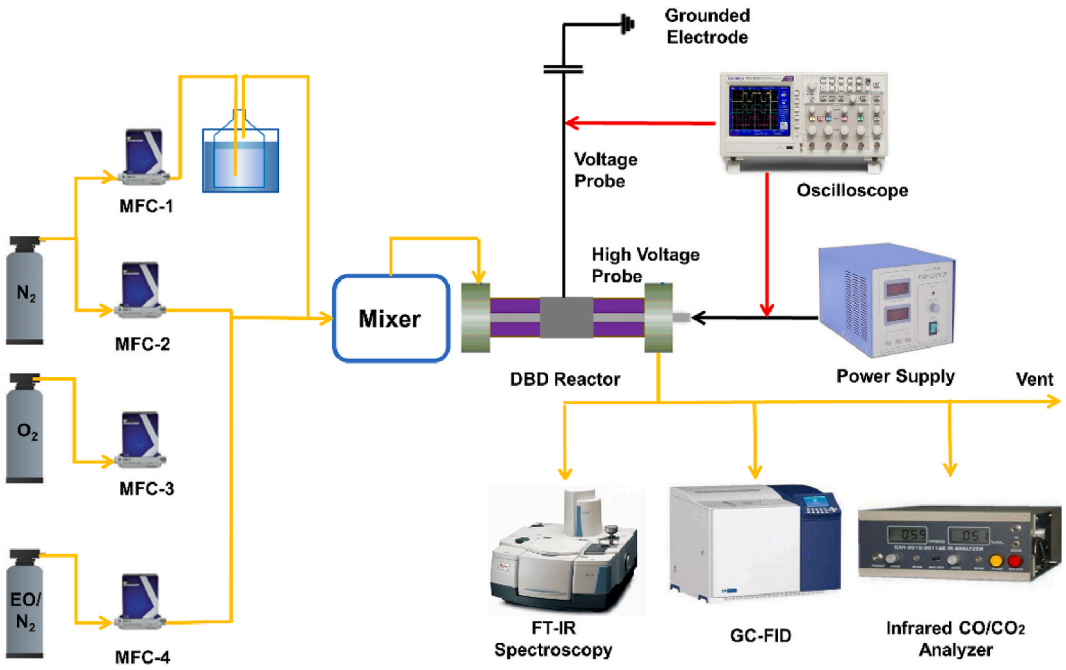

Fig. 1. Schematic diagram of the experimental setup.

into the plasma region and held in place by quartz wool. In addition, plasma oxidation of EO without a catalyst was also examined for comparison.

Fig. 2 depicts a typical *Q-U* Lissajous figure of DBD. The applied voltage across the reactor was assigned to the X-axis, while the charge across the measuring capacitor was assigned to the Y-axis. The effective capacitance of the DBD reactor (C_{eff}) can be calculated using the slope of the sidelines of the Lissajous figure [28]. The area of the Lissajous figure is proportional to the discharge power (P) of a DBD, which can be calculated as follows:

$$P(W) = f \times C_{ext} \times A \tag{1}$$

where C_{ext} is the external capacitance (0.47 μF), f is the discharge frequency (kept at 9.8 kHz) and A is the area of the Lissajous figure.

Specific energy input (SEI) was calculated by dividing the discharge power by the gas flow rate.

$$\text{SEI}\ \left(\text{J}\ \text{l}^{-1}\right) = \frac{P}{Q} \times 60 \tag{2}$$

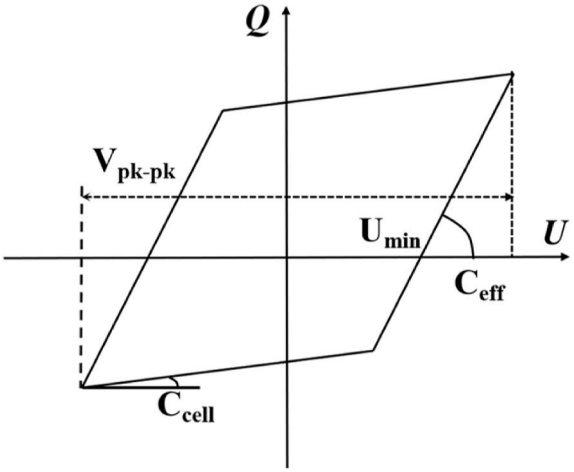

Fig. 2. Typical *Q-U* Lissajous figure for DBD plasma.

where Q is the total flow rate (l min^{-1}).

The breakdown voltage of the DBD reactor can be calculated as

$$U_b(\text{kV}) = \frac{U_{\min}}{1 + \frac{C_{eff}}{C_{cell}}} \tag{3}$$

where $U_{\min}$, C_{eff} and C_{cell} are the minimum voltage for plasma discharge, effective capacitance, and total capacitance of the DBD plasma reactor, respectively, which can be determined from the Lissajous figure [28].

The EO concentrations at the inlet and outlet of the plasma reactor were measured online using gas chromatography (GC9790II, Fuli Co. Ltd., China) equipped with a flame ionization detector (FID) and a CB-624 capillary column (30 m × 0.25 mm × 1.4 μm) (Puli Co. Ltd., China). The GC-FID is fitted with a 6-way valve and a 500 μL sampling loop and the on-line measurement was performed by changing the status of the 6-way valve. N_2 was used as the carrier gas in the GC-FID with a purity of >99.999%, while the temperature of the oven and the detector was 60 °C and 220 °C, respectively. The concentrations of CO and CO_2 were measured using a Fourier transform infrared (FTIR) analyzer (GXH3011A, Huayun, China) with an accuracy of ±3%. The outlet gaseous products of plasma-catalytic EO oxidation were analyzed by an online FTIR spectrometer (Nicolet iS20, Thermo-Fisher, USA) with a cell path of 2.4 m. The EO conversion, CO_2 selectivity, and carbon balance of the process were defined as follows:

$$\eta_{EO}(\%) = \frac{c_{in} - c_{out}}{c_{in}} \times 100\% \tag{4}$$

$$CO_2\ \text{selectivity}\ (\%) = \frac{c_{co_2}}{2 \times (c_{in} - c_{out})} \times 100\% \tag{5}$$

$$\text{Carbon balance}\ \left(\%\right) = \frac{2 \times c_{out} + c_{co} + c_{co_2}}{2 \times c_{in}} \times 100\% \tag{6}$$

where c_{in}, c_{out}, c_{co} and c_{co_2} are the inlet EO concentration (ppm), outlet EO concentration (ppm), outlet CO concentration (ppm) and outlet CO_2 concentration (ppm), respectively.

3. Results and discussions

3.1. Catalyst characterization

Table 1 shows the textural properties of the Fe–Mn-X catalysts. The doping of transition metal into the Fe–Mn catalyst had no significant effect on the specific surface area (S_{BET}) of the catalyst as the S_{BET} values for the Fe–Mn-X catalysts only slightly varied between 22.2 $m^2\ g^{-1}$ and 27.3 $m^2\ g^{-1}$, while the S_{BET} of the Fe–Mn catalyst was 19.8 $m^2\ g^{-1}$. In addition, the Fe–Mn–Ce and Fe–Mn–Co samples had higher S_{BET} values than Fe–Mn–Cu and Fe–Mn. Moreover, the pore volumes and average pore diameters of the Fe–Mn-X catalysts were slightly higher compared to the Fe–Mn catalyst, indicating a synergistic effect in textural properties between the doped element and the Fe–Mn sample [22,29]. The higher S_{BET} values of the Fe–Mn-X catalysts may offer more active sites for surface reactions.

The XRD patterns of the Fe–Mn catalyst show major diffraction peaks at 35.0°, 61.7° and 29.7° (in Fig. 3), indicating the existence of a cubic $Fe_3Mn_3O_3$ structure (PDF No.75–0034), while the weak broad diffraction around 62.4° could be attributed to the presence of α-Fe_2O_3 crystal phase (PDF No. 33–0664) on the Fe–Mn catalyst [19,30]. The XRD patterns of the Fe–Mn-X catalysts indicate that the doping of the transition metals of Ce, Co and Cu had a negligible influence on the crystalline structure of the parent Fe–Mn catalyst. Interestingly, the intensities of diffraction peaks of the Fe–Mn–Co and Fe–Mn–Cu catalysts were similar to those of Fe–Mn, whereas the intensities of diffraction peaks of Fe–Mn–Ce were much lower, indicating lower crystallinity. No obvious diffraction peaks of doped Ce, Co and Cu species were observed in the XRD patterns, revealing that the doped species were finely dispersed on the surfaces of Fe–Mn or incorporated into the crystalline of the cubic $Fe_3Mn_3O_8$ structure to form complex oxide [31]. Moreover, these results confirm that the incorporation of Ce, Co and Cu elements into the $Fe_3Mn_3O_3$ crystalline structure may result in structural defects due to the difference in ion radius between Fe, Mn and the dopants [32]. As a result, more oxygen vacancies are likely to form in the Fe–Mn-X catalysts [33].

Fig. 4a shows the XPS spectra of Fe 2p for all three Fe–Mn-X catalysts and the Fe–Mn catalyst. The peaks centered at 710.6 eV–711.0 eV are attributed to Fe $2p_{3/2}$, while the peaks at around 724.0 eV could be assigned to Fe $2p_{1/2}$. The Fe $2p_{3/2}$ spectra show two distinct peaks at 710.3 eV and 712.6 eV, which could be associated with the Fe^{2+} and Fe^{3+} species on the catalyst surfaces, respectively [19]. For all samples, the shake-up satellite peaks observed around 714.0 eV and 719.0 eV correspond to the Fe^{2+} and Fe^{3+} species, respectively [22]. Doping the Fe–Mn catalyst with Ce, Co and Cu slightly reduced the relative content of Fe^{3+} (Fe^{3+}/Fe_{total}) from 0.56 for Fe–Mn-X to 0.51–0.54 for Fe–Mn (Table 1). The variation in the relative content of Fe^{3+} indicates that some of the Fe^{3+} species were converted to Fe^{2+} by doping the Fe–Mn catalyst with Ce, Co, and Cu elements.

Fig. 4b depicts the XPS profiles of Mn 2p for the four catalysts. The binding energies of Mn $2p_{3/2}$ and Mn $2p_{1/2}$ are approximately 653.0 eV and 641.2 eV, respectively. Three major characteristic peaks at around 643.4 eV, 641.6 eV and 640.2 eV, could be attributed to the Mn^{4+}, Mn^{3+} and Mn^{2+} species, respectively [34,35]. The Fe–Mn-X catalysts had a relative concentration of Mn^{4+} (Mn^{4+}/Mn_{total}) in the range of 0.40–0.43, which was notably higher than the Fe–Mn catalyst (0.35), with Fe–Mn–Co having the highest relative concentration of Mn^{4+}.

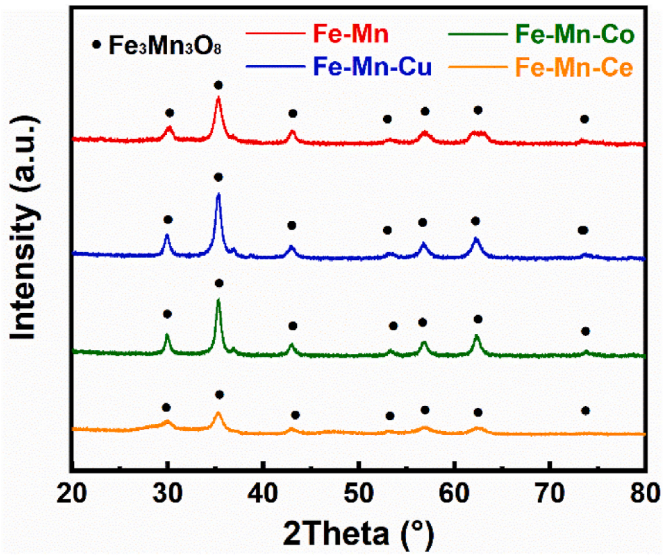

Fig. 3. XRD patterns of the Fe–Mn-X catalysts.

Previous study has shown that Mn species with a higher valence state are closely related to oxygen vacancies on the catalyst surface and may benefit oxidation by releasing adjacent surface adsorbed oxygen species [36]. The increase in the relative concentrations of the Mn^{4+} and Fe^{2+} species indicates the formation of Mn^{4+}-O-Fe^{2+} redox cycles since electron compensation is required to maintain the electroneutrality of the catalysts after Ce, Co and Cu doping [37]. Improved redox cycles may also contribute to enhanced oxygen mobility of the Fe–Mn-X catalysts.

As shown in Fig. 4c, the XPS spectra of O 1s could be fitted into two major peaks. The peak at around 529.7 eV can be assigned to the lattice oxygen species (O_{latt}), while the peak at 531.5 eV is attributed to surface adsorbed oxygen (O_{ads}) [38]. The doping of Ce, Co and Cu significantly improved the relative concentrations of O_{ads} ($O_{ads}/(O_{ads} + O_{latt})$) of the Fe–Mn-X catalysts when compared to the Fe–Mn catalyst. The Fe–Mn–Co catalyst showed the highest $O_{ads}/(O_{ads} + O_{latt})$ value of 0.39, followed by Fe–Mn–Ce (0.31), Fe–Mn–Cu (0.27) and Fe–Mn (0.24). The incorporation of Ce, Co and Cu into the crystal structure of the Fe–Mn catalyst resulted in an increase in the relative content of O_{ads}, indicating that more oxygen vacancies on the surface of the Fe–Mn-X catalysts. Oxygen vacancies are regarded as the oxygen adsorption and desorption centers [39]. The generated O_{ads} species are more effective than O_{latt} species in the oxidation of VOCs on catalyst surfaces due to their higher mobility than O_{latt} species. The presence of more O_{ads} on the catalyst surfaces may therefore benefit the oxidation process [14].

The H_2-TPR profile of the Fe–Mn catalyst (Fig. 5) showed overlapping reduction peaks at 365 °C, 450 °C and 560 °C, which correspond to the reduction of Fe^{3+} to Fe^{2+}, Mn^{4+} to Mn^{3+} and Mn^{3+} to Mn^{2+} species, respectively [20]. The doping of Ce, Co and Cu into the Fe–Mn catalyst significantly affected the reduction properties of the Fe–Mn-X catalysts, shifting the reduction peaks to lower temperatures. For example, the first reduction peak appeared at 242 °C over the Fe–Mn–Ce catalyst, while the second and the third reduction peaks located at 389 °C and 591 °C, respectively. The H_2-TPR profile of Fe–Mn–Co

Table 1
Physicochemical properties of the Fe–Mn-X catalysts.

Catalysts	S_{BET} ($m^2\ g^{-1}$)	Pore volume ($cm^3\ g^{-1}$)	Average pore diameter (nm)	Fe^{3+}/Fe_{total}	Mn^{4+}/Mn_{total}	$O_{ads}/(O_{ads} + O_{latt})$	H_2 consumption (mmol g^{-1})
Fe–Mn–Ce	27.3	0.08	8.8	0.54	0.36	0.27	14.8
Fe–Mn–Co	27.1	0.13	15.1	0.51	0.43	0.39	16.7
Fe–Mn–Cu	22.2	0.10	14.3	0.52	0.40	0.31	16.0
Fe–Mn	19.8	0.06	7.9	0.56	0.35	0.24	14.6

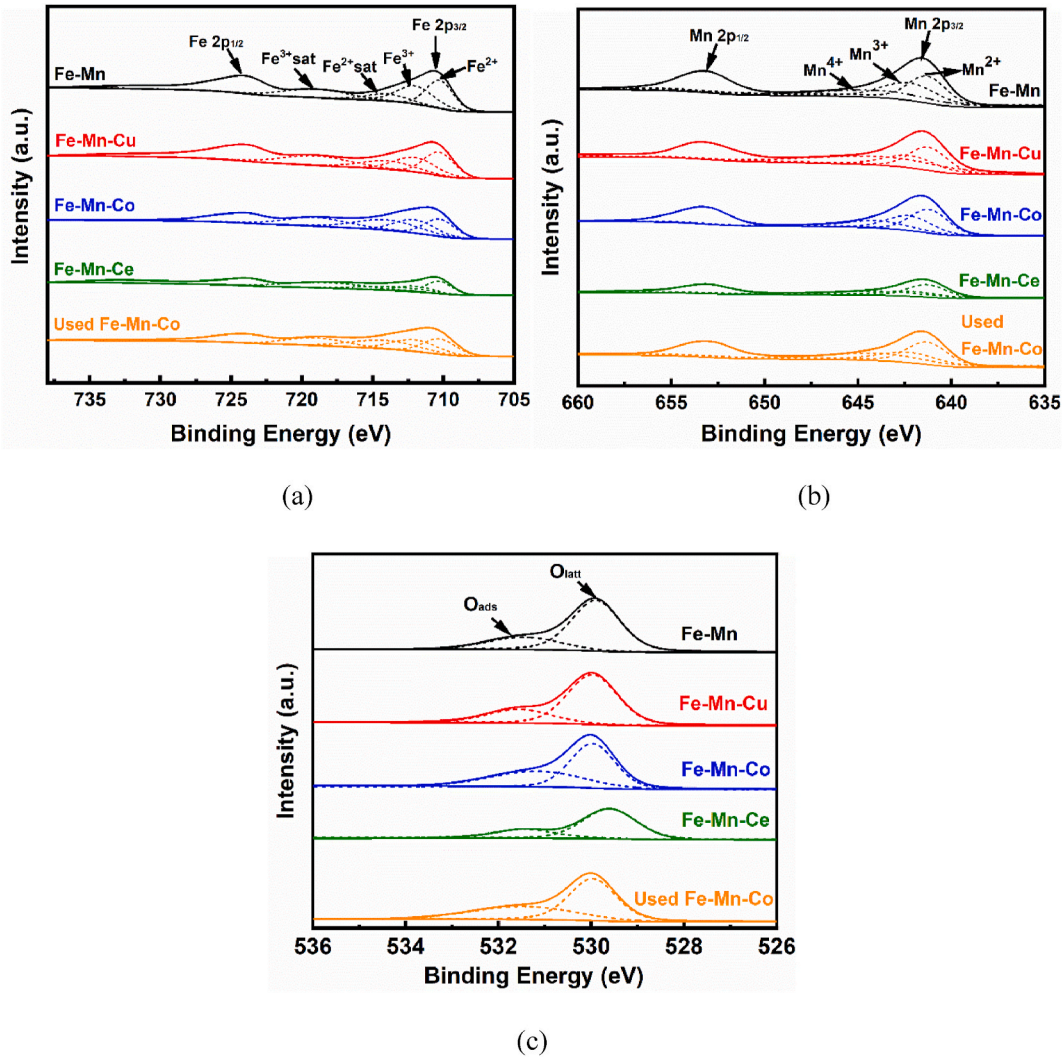

Fig. 4. XPS spectra of the Fe–Mn-X catalysts: (a) Fe 2p, (b) Mn 2p, (c) O 1s.

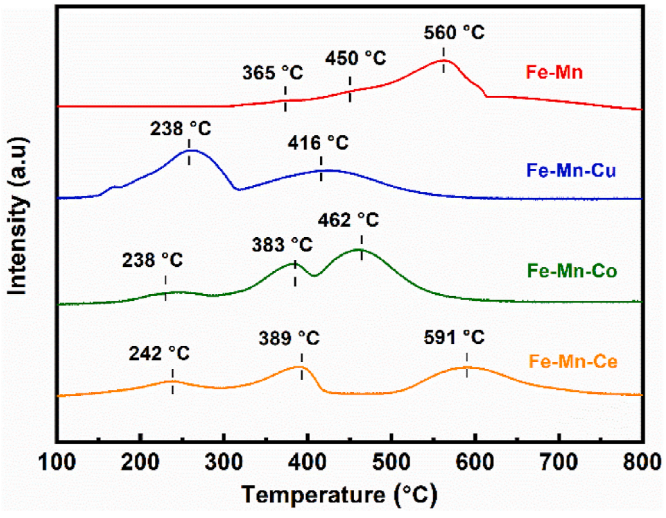

Fig. 5. H_2-TPR profiles of the Fe–Mn-X and Fe–Mn catalysts.

exhibited three distinct reduction peaks at 238 °C, 383 °C and 462 °C, while the Fe–Mn–Cu catalyst showed two broad reduction peaks at 258 °C and 416 °C. The lower reduction temperatures of the Fe–Mn-X catalysts indicate that the oxygen species on the catalyst surfaces can be reduced much more easily than the Fe–Mn catalyst, revealing that the mobility of oxygen species of the Fe–Mn-X was much higher than that of the Fe–Mn catalyst, which could be attributed to the mutual effect of various metal species [14,40]. The amount of H_2 consumption for each catalyst is listed in Table 1. The Fe–Mn–Co catalyst showed the highest H_2 consumption of 16.7 mmol g^{-1}, followed by the Fe–Mn–Cu (16.0 mmol g^{-1}) and Fe–Mn–Ce (14.8 mmol g^{-1}) catalysts, demonstrating the abundance of oxygen species with high mobility on the surfaces of the Fe–Mn–Co catalyst. To summarize, among the four catalysts under investigation, the Fe–Mn–Co catalyst had the best reducibility and would favor the oxidation of adsorbed pollutants and intermediates on the catalyst surfaces [17].

3.2. Discharge characteristics

Fig. 6 presents the Lissajous figures of plasma discharge with and without catalysts at an SIE of 612.7 J l^{-1}. The shape of the Lissajous figure changed slightly from parallelogram for plasma only to oval for the plasma-catalytic system, indicating a change in discharge mode in the presence of the Fe–Mn-X and Fe–Mn catalysts [41]. Packing the catalysts into the plasma zone enabled the transition of plasma discharge from filamentary discharge to a combination of surface discharge on the catalyst surface and spatially limited micro-discharges generated in the void spaces between the reactor wall and catalyst particles [28]. As

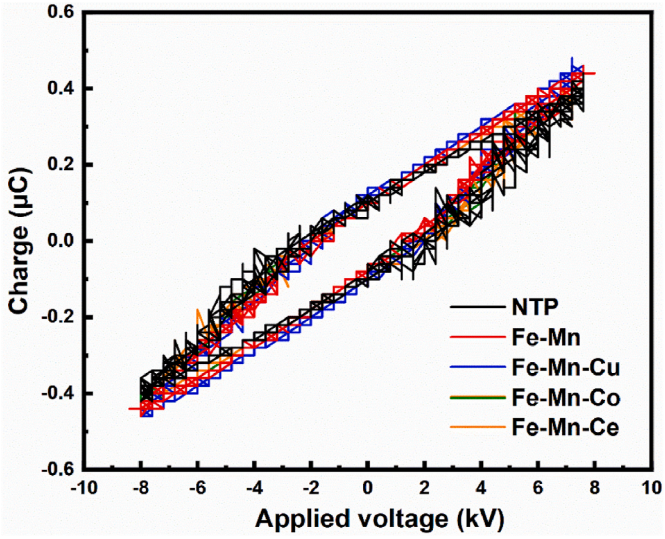

Fig. 6. Lissajous figures of plasma discharge with and without a catalyst at an SEI of 612.7 J l^{-1}.

shown in Fig. 6, the peak-to-peak voltage (V_{pk-pk}) was around 14.4 kV regardless of catalyst type, but increased to 15.2 kV in the plasma only system. The DBD reactor packed with Fe–Mn-X had a breakdown voltage of around 0.82 kV, which was slightly lower than the plasma only system (0.97 kV). The presence of the Fe–Mn-X catalyst in the DBD reactor would significantly reduce the discharge volume, resulting in a reduction of the equivalent discharge gap of the plasma-catalytic system. Thus, the coupling of DBD with the catalysts can enhance the average electric field of the discharge, producing more reactive species for the reaction [42,43]. Furthermore, the C_{eff} value was in the following order: Fe–Mn–Co (74.8 pF) > Fe–Mn–Ce (74.4 pF) > Fe–Mn–Cu (72.5 pF) > Fe–Mn (70.6 pF) > plasma only (67.6 pF). Higher C_{eff} values indicate that more power can be injected into the plasma per discharge cycle for plasma-induced chemical reactions [44,45].

3.3. Plasma-catalytic oxidation of EO

3.3.1. Effect of catalysts

Fig. 7 presents the influence of SEI on the conversion of EO and CO_2 selectivity with and without catalysts. Both EO conversion and CO_2 selectivity increased with the increasing SEI irrespective of the catalyst composition. In the plasma-only system, increasing the SEI from 376.4 J l^{-1} to 694.9 J l^{-1} doubled the EO conversion from 30.9% to 68.0% along with the enhanced CO_2 selectivity from 27.0% to 34.9%. In the presence of the Fe–Mn catalyst, varying the SEI from 376.6 J l^{-1} to 640.6 J l^{-1} considerably enhanced EO conversion from 45.8% to 67.3% and CO_2 selectivity from 51.7% to 70.5%. The carbon balance increased from 66.9% to 74.7% in the reaction using plasma only when SEI increased from 376.6 J l^{-1} to 640.6 J l^{-1}. It is well recognized that increasing SEI at a constant frequency typically increases the number of micro-discharges in DBDs, which could result in the production of more chemically reactive species via effective collisions between energetic electrons and gas molecules (*e.g.*, N_2 and O_2). As a result, these chemically reactive species would contribute to enhanced oxidation of EO and organic intermediates, as well as the formation of more CO_2, resulting in improved CO_2 selectivity and carbon balance of the plasma process [46].

Compared to the oxidation of EO using plasma only, the combination of DBD with Fe–Mn or Fe–Mn-X notably improved EO conversion and CO_2 selectivity. For example, packing Fe–Mn into the DBD reactor improved EO conversion by ~6.0% and almost doubled CO_2 selectivity at an SEI of 640.6 J l^{-1} when compared with the plasma-only system. The addition of a metal dopant to the Fe–Mn catalyst further enhanced plasma-catalytic EO oxidation. The highest EO conversion of 91.9% and CO_2 selectivity of 78.9% were obtained using the Fe–Mn–Co catalyst at an SEI of 730.3 J l^{-1}. For a given SEI, EO conversion followed the order Fe–Mn–Co > Fe–Mn–Ce > Fe–Mn–Cu > Fe–Mn > plasma only. In addition, the CO_2 selectivity of plasma-catalyzed EO oxidation process followed the same order as EO conversion. Similarly, the presence of a Fe–Mn-X catalyst slightly improved the carbon balance of the process by 3.0%–14.1% when compared to using plasma only in the same SEI range. The type of metal dopant in the Fe–Mn-X catalysts had a significant impact on the reaction performance of plasma-catalytic EO oxidation. Catalyst characterizations confirm that the textural properties of the Fe–Mn-X catalysts after metal doping were similar to those of the Fe–Mn catalyst. However, the doped Ce, Co and Cu species can dissolve into the crystal structure of $Fe_3Mn_3O_8$. Due to the different ionic radii of Fe, Mn, Ce, Co and Cu species, the crystal structure of $Fe_3Mn_3O_8$ would contract or expand, resulting in the formation of oxygen vacancies on the catalyst surfaces [19,33]. In addition, the Fe–Mn–Co catalyst showed the highest Mn^{4+}/Mn_{total} and $O_{ads}/(O_{ads} + O_{latt})$ values, indicating that this catalyst possessed the most oxygen vacancies and the highest mobility of oxygen species among the tested catalysts [47]. This finding is consistent with the superior reducing capacity of the Fe–Mn–Co catalyst when compared to other tested catalysts, as demonstrated by H_2-TPR profiles. Furthermore, the presence of more active oxygen species can promote catalytic EO oxidation in the presence of plasma discharge, which can improve CO_2 selectivity and carbon balance of the process due to enhanced oxidation of the organic intermediates to gaseous products of CO, CO_2 and H_2O.

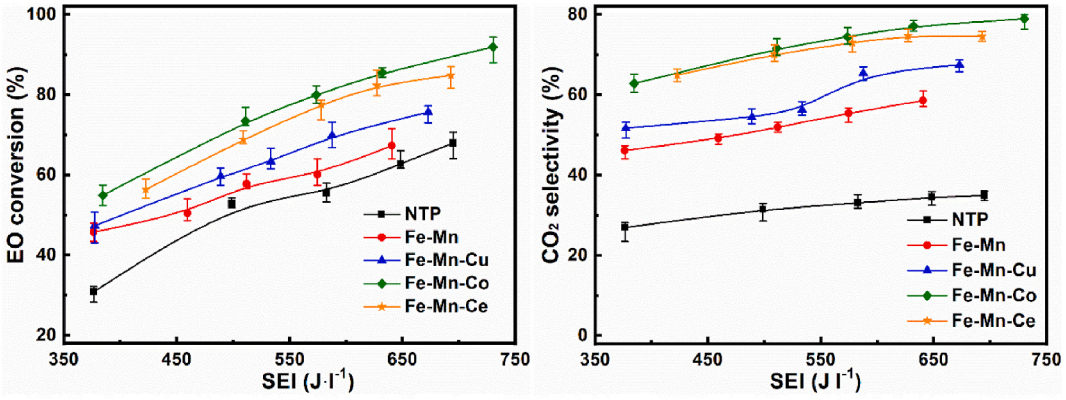

Fig. 7. Plasma-catalytic oxidation of EO over the Fe–Mn-X catalysts: (a) EO conversion and (b) CO_2 selectivity.

3.3.2. Effect of relative humidity

Due to the presence of water vapor in most industrial waste gas streams, the effect of relative humidity (RH) on plasma-catalytic EO oxidation was investigated in this study. Fig. 8 shows the effect of RH on EO oxidation using plasma only and over the Fe–Mn–Co catalyst at an SEI of 612.7 J l^{-1}. The results show that increase the RH initially increased the EO conversion and reached a peak at an RH of 60%, while further increasing the RH to 80% decreased the conversion of EO. For instance, in the plasma-only system, varying the RH from 0 to 60% enhanced EO conversion from 58.5% to 80.5%, when further raising the RH from 60% to 80% reduced the conversion of EO to 76.6%. In the plasma-catalytic oxidation over the Fe–Mn–Co catalyst, the EO conversion increased from 76.3% to 89.4% in the RH range of 0–60%, while it declined to 85.4% at 80% RH. Raising the RH from 0 to 80% increased CO_2 selectivity from 33.9% to 47.1% for plasma only and from 50.2% to 64.6% for plasma coupled with Fe–Mn–Co, respectively. The carbon balance increased from 86.1% to 98.8% in the plasma-catalyzed oxidation of EO over the Fe–Mn–Co catalyst in the presence of water vapor, whereas in the plasma-only system, the carbon balance increased from 71.2% to 83.1% with an increase in the RH from 0 to 60%, while further increasing the RH decreased the carbon balance by 4%–5%.

It is well known that water molecules can be dissociated by energetic electrons to generate OH radicals in a plasma environment [48,49]:

$$e + H_2O \rightarrow OH + H + e$$

OH radicals are highly oxidative, and they can react with EO, reaction intermediates and various by-products towards deep oxidation. OH radicals have a much higher oxidation potential than O radicals [50]. As a result, increasing RH improved EO conversion, CO_2 selectivity and carbon balance. However, since H_2O molecules possess a high electronegativity, the attachment of energetic electrons by excess water molecules is likely to occur at a higher RH [51]. Thus, the number density of electrons and mean electron energy would be decreased, resulting in reduced EO oxidation [52]. Previous work reported that water molecules could be adsorbed onto the catalyst surfaces to form the first and second H_2O monolayer at ~15% and 30–40% RH, respectively [53]. Since the water content of the carrier gas is orders of magnitude higher than that of the EO molecules, an increase in RH would result in the occupation of active sites on catalyst surfaces by water molecules due to competitive adsorption. At higher RH values, the adsorption of EO molecules and intermediates would be inhibited. Consequently, the EO conversion was also reduced at higher RH levels. A similar phenomenon was reported in previous work, *e.g.,* benzene oxidation in the plasma-catalytic system over Ag–Ce/γ-Al_2O_3 [54].

3.3.3. By-products and reaction mechanisms

FTIR was used to examine the effluent from plasma-catalytic EO oxidation with and without Fe–Mn–Co. To ensure the generation of detectable by-products, the initial EO concentration and SEI were fixed at 500 ppm and 612.7 J l^{-1}, respectively, during the FTIR measurement. As shown in Fig. 9, major organic by-products in plasma-catalytic EO oxidation include CH_3CHO, C_2H_6, C_2H_5OH and CH_4 under all reaction conditions. The addition of Fe–Mn–Co to the plasma reactor considerably affected by-product distribution. We found that the plasma-catalyst coupling enhanced the peak intensity of CO_2 but had no effect on the peak intensities of other detected by-products, which is consistent with the enhanced CO_2 selectivity and higher EO conversion in the plasma-catalytic system using Fe–Mn–Co. Regardless of the presence of the Fe–Mn–Co catalyst, the presence of 20% RH in the carrier gas significantly lowered the peak intensities of EO while increasing the peak intensities of CO_2 in the FTIR spectra. These findings imply that deeper oxidation of EO occurred during the plasma process in the presence of water vapor. Moreover, the presence of 20% RH reduced the peak intensities of major by-products such as CH_3CHO, C_2H_6, and C_2H_5OH, while increasing the peak intensities of CH_4.

In a DBD plasma, the energetic electrons typically have electron temperatures ranging from 1 to 10 eV [55]. These electrons could directly collide with the EO molecules as well as various EO fragments such as CH_2CHO, CH_2CH_2, CH_2OCH_2, CH_2O and CH_2 through the rupture of C–H (4.23 eV), C–O (3.40 eV) and C–C (3.62 eV) chemical bonds of EO [41,56]. On the other hand, EO and its fragments could be oxidized by chemically reactive species such as O, O_3 and OH to produce harmless final products such as CO_2 and H_2O. When introducing water vapor into the reaction, a portion of the energetic electrons would be diminished by collisions due to the high electronegativity of H_2O molecules, which may inhibit the oxidation of EO, particularly under higher RH conditions [57].

In the presence of the Fe–Mn-X catalysts, the discharge gap was reduced when compared to the plasma-only system. As a result, the discharge region was expanded, and the discharge mode was changed to a combination of surface and gas-phase discharge [41]. Meanwhile, the amount of energy dissipated into the DBD reactor for EO oxidation has been increased. More reactive species can be generated and contribute to the oxidation of EO and reaction intermediates, especially in conditions of dry air and low RH. In the plasma-catalytic system, the oxidation of EO could occur both in the gas phase and on the catalyst surfaces. Since the catalyst pellets were placed directly in the plasma region, the radicals generated near/on the interfaces between the catalyst surface

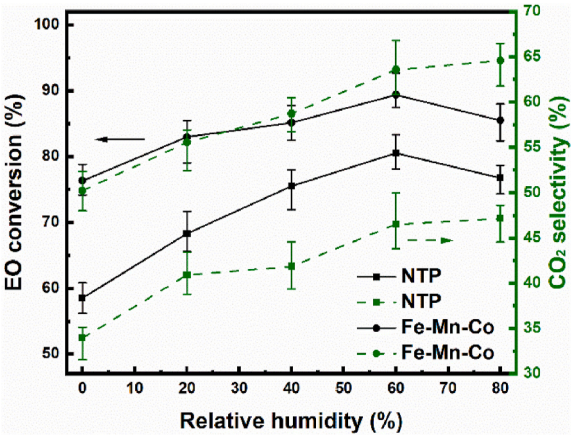

Fig. 8. Effect of RH on plasma-catalytic EO oxidation over Fe–Mn–Co at an SEI of 612.7 J l^{-1} (solid line: EO conversion; dashed line: CO_2 selectivity).

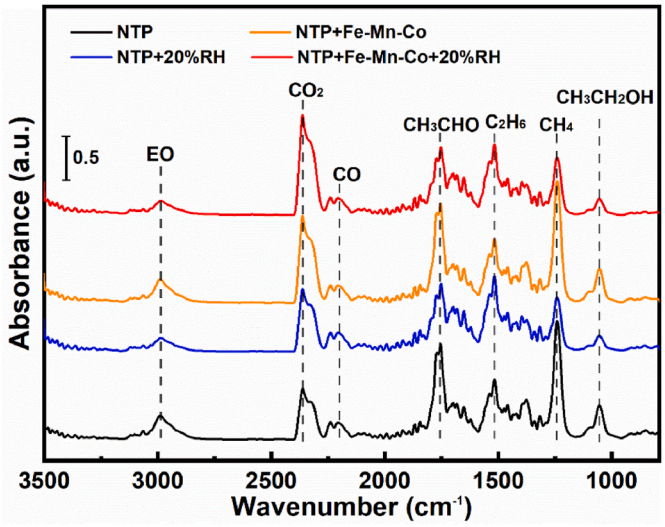

Fig. 9. FTIR spectra of plasma-induced EO oxidation under different reaction conditions at an SEI of 612.7 J l^{-1}.

and the gas-phase could be transported onto the catalyst surface along with EO molecules and reaction intermediates [58]. Neyts et al. reported that rotationally and vibrationally excited species generated in the plasma region may enhance the adsorption capacity of catalysts at low temperatures, extending the residence time of these species on catalyst surfaces and increasing the possibility of effective collisions between the reactants for EO oxidation [59].

After doping with Ce, Co and Cu, the S_{BET} of the catalysts increased by 12.1%–37.9%, indicating that more active sites can be provided for the adsorption of reactants. Once adsorbed, EO molecules, reaction intermediates and radicals could be oxidized to produce the desired end products. According to XPS spectra, the Fe^{3+} sites were reduced to Fe^{2+} after doping with Ce, Co and Cu, while part of the reduced Mn species was oxidized to Mn^{4+}, indicating that the Fe–Mn-X catalysts formed more oxygen vacancies than the Fe–Mn catalyst [39,60]. Oxygen vacancies are regarded as the adsorption-desorption centers for O_{ads} species, with the order of $O_{ads}/(O_{ads} + O_{latt})$ and Mn^{4+}/Mn_{total} being the same in this work. As a result, the Fe–Mn–Co catalyst generated the highest $O_{ads}/(O_{ads} + O_{latt})$ value.

The redox cycles between Fe^{3+}/Fe^{2+} and $Mn^{4+}/Mn^{3+}/Mn^{2+}$ of the Fe–Mn catalysts would be involved in the electron transfer process during the plasma-catalytic EO oxidation, promoting the reducibility of the Fe–Mn-X catalysts and enabling O_{ads} to be released (mainly existing on oxygen vacancies) much more easily [25]. The lowest reduction temperature and highest H_2 consumption amount of Fe–Mn–Co confirm the enhanced reducibility of the Fe–Mn-X catalysts. The released O_{ads} species with high mobility could react with adjacent adsorbed EO molecules and intermediates, resulting in superior catalytic performance in plasma environment for deep EO oxidation, as evidenced by the slight decreased $O_{ads}/(O_{ads} + O_{latt})$ value of the used Fe–Mn–Co catalyst compared to the fresh sample [39]. Moreover, the oxygen vacancies in the catalyst would be refilled by O radicals generated in plasma or O_2 molecules. As a result, organic by-products could be oxidized in the plasma-catalytic system, thereby enhancing CO_2 selectivity.

4. Conclusions

In this work, plasma-catalyzed EO oxidation over Fe–Mn based ternary catalysts was investigated in a DBD reactor. Compared to the Fe–Mn catalyst, packing Fe–Mn-X catalysts into the plasma zone enhanced the conversion of EO and CO_2 selectivity. At an SEI of 730.2 J l^{-1}, the highest EO conversion of 91.9% and CO_2 selectivity of 78.9% were achieved using the Fe–Mn–Co catalyst. The incorporation of Ce, Co and Co into the Fe–Mn catalyst increased the specific surface area and O_{ads} content on the catalyst surfaces while maintaining the crystalline of the Fe–Mn catalyst. As a result, the redox properties of the Fe–Mn-X catalysts were enhanced, which contributes to the deep oxidation of EO and organic intermediates in the plasma-catalytic process. The presence of water vapor in the plasma-catalytic system improved the conversion of EO from 76.3% to 89.4% as the RH increased from 0 to 60%. However, further increasing the RH to 80% reduced the conversion of EO. In contrast, the CO_2 selectivity increased with the RH across the examined range. The reaction mechanism of plasma-catalyzed EO oxidation was discussed based on the analysis of the organic by-products.

Data availability

The data supporting the findings of this study are available from the corresponding authors upon reasonable request.

Declaration of competing interest

The authors declare that they have no known competing financial interests or personal relationships that could have appeared to influence the work reported in this paper.

Acknowledgements

X. Zhu acknowledges funding from the National Natural Science Foundation of China (No. 51976093) and K. C. Wong Magna Fund at Ningbo University. Y. Jiang acknowledges support from Qingdao Science and Technology Demonstration and Guidance Project for Benefiting the People (Grant number 21-1-4-sf-8-nsh). X. Tu gratefully acknowledges the support from the Engineering and Physical Sciences Research Council (EP/V036696) and the British Council Newton Fund Institutional Links Grant (No. 623389161).

References

[1] A. Ikhlaq, B. Kasprzyk-Hordern, Catalytic ozonation of chlorinated VOCs on ZSM-5 zeolites and alumina: formation of chlorides, Appl. Catal. B Environ. 200 (2017) 274–282.
[2] Z. Zhang, Z. Jiang, W. Shangguan, Low-temperature catalysis for VOCs removal in technology and application: a state-of-the-art review, Catal. Today 264 (2016) 270–278.
[3] Y. Han, Y. Wang, F. Chai, J. Ma, L. Li, Biofilters for the co-treatment of volatile organic compounds and odors in a domestic waste landfill site, J. Clean. Prod. 277 (2020), 124012.
[4] W.-C. Chung, D.-H. Mei, X. Tu, M.-B. Chang, Removal of VOCs from gas streams via plasma and catalysis, Catal. Rev. Sci. Eng. 61 (2019) 270–331.
[5] A. Bogaerts, X. Tu, J.C. Whitehead, G. Centi, L. Lefferts, O. Guaitella, et al., The 2020 plasma catalysis roadmap, J. Phys. D Appl. Phys. 53 (2020), 443001.
[6] X. Zhang, B. Ren, Y. Xu, X. Li, P. Yu, Y. Sun, et al., Catalytic oxidation of toluene in air using manganese incorporated catalyst by non-thermal plasma system, Separ. Purif. Technol. 257 (2021), 117973.
[7] G. Chen, X. Tu, G. Homm, A. Weidenkaff, Plasma pyrolysis for a sustainable hydrogen economy, Nat. Rev. Mater. 7 (2022) 333–334.
[8] X. Zhu, J. Liu, X. Hu, Z. Zhou, X. Li, W. Wang, et al., Plasma-catalytic synthesis of ammonia over Ru-based catalysts: insights into the support effect, J. Energy Inst. 102 (2022) 240–246.
[9] T. Chang, C. Ma, Z. Shen, S.K.P. Veerapandian, Y. Huang, N. De Geyter, et al., Mn-based catalysts for post non-thermal plasma catalytic abatement of VOCs: a review on experiments, simulations and modeling, Plasma Chem. Plasma Process. 41 (2021) 1239–1278.
[10] F. Saleem, A.H. Khoja, J. Umer, F. Ahmad, S.Z. Abbas, K. Zhang, et al., Removal of benzene as a tar model compound from a gas mixture using non-thermal plasma dielectric barrier discharge reactor, J. Energy Inst. 96 (2021) 97–105.
[11] Y. Sun, J. Wu, Y. Wang, J. Li, N. Wang, J. Harding, et al., Plasma-catalytic CO_2 Hydrogenation over a Pd/zno Catalyst: *in Situ* Probing of Gas-phase and Surface Reactions, JACS Au, 2022. In press, https://pubs.acs.org/doi/full/10.1021/jacsau.2c00028.
[12] M. Ronda-Lloret, Y. Wang, P. Oulego, G. Rothenberg, X. Tu, N.R. Shiju, CO_2 hydrogenation at atmospheric pressure and low temperature using plasma-enhanced catalysis over supported cobalt oxide catalysts, ACS Sustain. Chem. Eng. 8 (2020) 17397–17407.
[13] S.K.P. Veerapandian, N. De Geyter, J.-M. Giraudon, J.-F. Lamonier, R. Morent, The use of zeolites for VOCs abatement by combining non-thermal plasma, adsorption, and/or catalysis: a review, Catalysts 9 (2019) 98.
[14] N. Jiang, C. Qiu, L. Guo, K. Shang, N. Lu, J. Li, et al., Plasma-catalytic destruction of xylene over Ag-Mn mixed oxides in a pulsed sliding discharge reactor, J. Hazard Mater. 369 (2019) 611–620.
[15] C. Norsic, J.-M. Tatibouët, C. Batiot-Dupeyrat, E. Fourré, Non-thermal plasma assisted catalysis of methanol oxidation on Mn, Ce and Cu oxides supported on γ-Al_2O_3, Chem. Eng. J. 304 (2016) 563–572.
[16] Y. Liu, L. Lian, W. Zhao, R. Zhang, H. Hou, DBD coupled with MnO_x/γ-Al_2O_3 catalysts for the degradation of chlorobenzene, Plasma Sci. Technol. 22 (2020), 034016.
[17] Y. Cai, X. Zhu, W. Hu, C. Zheng, Y. Yang, M. Chen, et al., Plasma-catalytic decomposition of ethyl acetate over $LaMO_3$ (M = Mn, Fe, and Co) perovskite catalysts, J. Ind. Eng. Chem. 70 (2019) 447–452.
[18] N. Jiang, Y. Zhao, C. Qiu, K. Shang, N. Lu, J. Li, et al., Enhanced catalytic performance of CoO-CeO_2 for synergetic degradation of toluene in multistage sliding plasma system through response surface methodology (RSM), Appl. Catal. B Environ. 259 (2019), 118061.
[19] J. Mei, Y. Shen, Y. Li, S. Zhang, Y. Shen, W. Li, et al., Combined experimental and theoretical study of o-xylene elimination on Fe-Mn oxides catalysts, Chemosphere 292 (2022), 133442.
[20] Y. Zhou, S. Ren, M. Wang, J. Yang, Z. Chen, L. Chen, Mn and Fe oxides co-effect on nanopolyhedron CeO_2 catalyst for NH_3-SCR of NO, J. Energy Inst. 99 (2021) 97–104.
[21] F. Lu, J. Huang, Q. Wu, Y. Zhang, Mixture of α-Fe_2O_3 and MnO_2 powders for direct conversion of syngas to light olefins, Appl. Catal. Gen. 621 (2021), 118213.
[22] T. Chang, Z. Shen, C. Ma, J. Lu, Y. Huang, S.K.P. Veerapandian, et al., Process optimization of plasma-catalytic formaldehyde removal using MnO_x–Fe_2O_3 catalysts by response surface methodology, J. Environ. Chem. Eng. 9 (2021), 105773.

[23] L. Qin, B. Zhao, W. Chen, X. Liu, J. Han, Refluxing-coprecipitation to synthesize Fe_x−Mn_y/γ-Al_2O_3 catalyst for toluene removal in a nonthermal plasma-catalysis reactor, Mol. Catal. 517 (2022), 112023.
[24] S. Tang, X. Li, C. Zhang, Y. Liu, W. Zhang, D. Yuan, Strengthening decomposition of oxytetracycline in DBD plasma coupling with Fe-Mn oxide-loaded granular activated carbon, Plasma Sci. Technol. 21 (2019), 025504.
[25] H. Xiong, X. Zhu, S. Lu, C. Zhou, W. Xu, Z. Zhou, Enhancement of plasma-catalytic oxidation of ethylene oxide (EO) over Fe-Mn catalysts in a dielectric barrier discharge reactor, Sci. Total Environ. 788 (2021), 147675.
[26] N. Parvizi, N. Rahemi, S. Allahyari, M. Tasbihi, Plasma-catalytic degradation of BTX over ternary perovskite-type La_{1-x}(Co, Zn, Mg, Ba)$_x$$MnO_3$ nanocatalysts, J. Ind. Eng. Chem. 84 (2020) 167–178.
[27] W.T. Liao, W.J. Lee, C.Y. Chen, M. Shih, Decomposition of ethylene oxide in the RF plasma environment, Environ. Technol. 22 (2001) 165–173.
[28] X. Tu, H.J. Gallon, M.V. Twigg, P.A. Gorry, J.C. Whitehead, Dry reforming of methane over a Ni/Al_2O_3 catalyst in a coaxial dielectric barrier discharge reactor, J. Phys. D Appl. Phys. 44 (2011), 274007.
[29] S.-B. Fan, P.M. Kouotou, J.-J. Weng, G.-F. Pan, Z.-Y. Tian, Investigation on the structure stability and catalytic activity of Cu–Co binary oxides, Proc. Combust. Inst. 36 (2017) 4375–4382.
[30] P. Mungse, G. Saravanan, S. Rayalu, N. Labhsetwar, Mixed oxides of iron and manganese as potential low-cost oxygen carriers for chemical looping combustion, Energy Technol.: Ger. 3 (2015) 856–865.
[31] X. Jiang, X. Li, J. Wang, D. Long, L. Ling, W. Qiao, Three-dimensional Mn–Cu–Ce ternary mixed oxide networks prepared by polymer-assisted deposition for HCHO catalytic oxidation, Catal. Sci. Technol. 8 (2018) 2740–2749.
[32] X. Zhang, D. Wu, Ceramic monolith supported Mn–Ce–M ternary mixed-oxide (M=Cu, Ni or Co) catalyst for VOCs catalytic oxidation, Ceram. Int. 42 (2016) 16563–16570.
[33] M.R. Morales, F.N. Agüero, L.E. Cadus, Catalytic combustion of n-hexane over alumina supported Mn–Cu–Ce catalysts, Catal. Lett. 143 (2013) 1003–1011.
[34] D. Wang, L. Jin, Y. Li, B. Wei, D. Yao, H. Hu, Upgrading of vacuum residue with chemical looping partial oxidation over Fe-Mn mixed metal oxides, Fuel 239 (2019) 764–773.
[35] J. Tan, Y. Wei, Y. Sun, J. Liu, Z. Zhao, W. Song, et al., Simultaneous removal of NO_x and soot particulates from diesel engine exhaust by 3DOM Fe–Mn oxide catalysts, J. Ind. Eng. Chem. 63 (2018) 84–94.
[36] J. Ling, Y. Dong, P. Cao, Y. Wang, Y. Li, Preparation of Mn-Fe oxide by a hydrolysis-driven redox method and its application in formaldehyde oxidation, ACS Omega 6 (2021) 23274–23280.
[37] M. Zhang, D. Yin, J. Guo, H. Wu, M. Gong, X. Feng, Ternary catalyst Mn-Fe-Ce/Al_2O_3 for the ozonation of phenol pollutant: performance and mechanism, Environ. Sci. Pollut. Res. Int. 28 (2021) 32921–32932.
[38] G. Wei, Q. Zhang, D. Zhang, J. Wang, T. Tang, H. Wang, et al., The influence of annealing temperature on copper-manganese catalyst towards the catalytic combustion of toluene: the mechanism study, Appl. Surf. Sci. 497 (2019), 143777.
[39] X. Zhu, X. Gao, R. Qin, Y. Zeng, R. Qu, C. Zheng, et al., Plasma-catalytic removal of formaldehyde over Cu–Ce catalysts in a dielectric barrier discharge reactor, Appl. Catal. B Environ. 170–171 (2015) 293–300.
[40] H. Li, G. Lu, Q. Dai, Y. Wang, Y. Guo, Y. Guo, Efficient low-temperature catalytic combustion of trichloroethylene over flower-like mesoporous Mn-doped CeO_2 microspheres, Appl. Catal. B Environ. 102 (2011) 475–483.
[41] C. Zheng, X. Zhu, X. Gao, L. Liu, Q. Chang, Z. Luo, et al., Experimental study of acetone removal by packed-bed dielectric barrier discharge reactor, J. Ind. Eng. Chem. 20 (2014) 2761–2768.
[42] J. Liu, X. Zhu, X. Hu, X. Tu, Plasma-assisted ammonia synthesis in a packed-bed dielectric barrier discharge reactor: roles of dielectric constant and thermal conductivity of packing materials, Plasma Sci. Technol. 24 (2022), 110786.
[43] Y. Wang, M. Craven, X. Yu, J. Ding, P. Bryant, J. Huang, et al., Plasma-enhanced catalytic synthesis of ammonia over a Ni/Al_2O_3 catalyst at near-room temperature: insights into the importance of the catalyst surface on the reaction mechanism, ACS Catal. 9 (2019) 10780–10793.
[44] Y. Zeng, X. Tu, Plasma-catalytic hydrogenation of CO_2 for the cogeneration of CO and CH_4in a dielectric barrier discharge reactor: effect of argon addition, J. Phys. D Appl. Phys. 50 (2017), 184004.
[45] R. Aerts, W. Somers, A. Bogaerts, Carbon dioxide splitting in a dielectric barrier discharge plasma: a combined experimental and computational study, ChemSusChem 8 (2015) 702–716.
[46] B. Wang, C. Chi, M. Xu, C. Wang, D. Meng, Plasma-catalytic removal of toluene over CeO_2-MnO_x catalysts in an atmosphere dielectric barrier discharge, Chem. Eng. J. 322 (2017) 679–692.
[47] Y. Wang, G. Wang, W. Deng, J. Han, L. Qin, B. Zhao, et al., Study on the structure-activity relationship of Fe-Mn oxide catalysts for chlorobenzene catalytic combustion, Chem. Eng. J. 395 (2020), 125172.
[48] A.M. Vandenbroucke, R. Morent, N. De Geyter, C. Leys, Non-thermal plasmas for non-catalytic and catalytic VOC abatement, J. Hazard Mater. 195 (2011) 30–54.
[49] K.A. Abedi, F. Ghorbani-Shahna, A. Bahrami, H. Ebrahimi, A. Maleki, F. Madjidi, et al., Effect of TiO_2/GAC and water vapor on chloroform decomposition in a hybrid plasma-catalytic system, Environ. Technol. 39 (2018) 2041–2050.
[50] X. Zhu, X. Gao, C. Zheng, Z. Wang, M. Ni, X. Tu, Plasma-catalytic removal of a low concentration of acetone in humid conditions, RSC Adv. 4 (2014) 37796–37805.
[51] Y. Wang, Z. Liao, S. Mathieu, F. Bin, X. Tu, Prediction and evaluation of plasma arc reforming of naphthalene using a hybrid machine learning model, J. Hazard Mater. 404 (2021), 123965.
[52] J.-S. Chang, Y. Uchida, K. Urashima, R. Taylor, Transient barrier discharge characteristics of parallel-plate-type, packed-bed, non-thermal plasma reactor under high-humidity conditions, Plasma Process. Polym. 3 (2006) 721–726.
[53] X. Deng, T. Herranz, C. Weis, H. Bluhm, M. Salmeron, Adsorption of water on Cu_2O and Al_2O_3 thin films, J. Phys. Chem. C 112 (2008) 9668–9672.
[54] N. Jiang, J. Hu, J. Li, K. Shang, N. Lu, Y. Wu, Plasma-catalytic degradation of benzene over Ag–Ce bimetallic oxide catalysts using hybrid surface/packed-bed discharge plasmas, Appl. Catal. B Environ. 184 (2016) 355–363.
[55] E.C. Neyts, Plasma-surface interactions in plasma catalysis, Plasma Chem. Plasma Process. 36 (2015) 185–212.
[56] L. Magne, N. Blin-Simiand, K. Gadonna, P. Jeanney, F. Jorand, S. Pasquiers, et al., OH kinetics in photo-triggered discharges used for VOCs conversion, Eur. Phys. J. Appl. Phys. 47 (2009), 22816.
[57] Y. Itikawa, N. Mason, Cross sections for electron collisions with water molecules, J. Phys. Chem. Ref. Data 34 (2005) 1–22.
[58] P.-A. Maitre, M.S. Bieniek, P.N. Kechagiopoulos, Plasma-enhanced catalysis for the upgrading of methane: a review of modelling and simulation methods, Reaction Chem. Eng. 5 (2020) 814–837.
[59] E.C. Neyts, A. Bogaerts, Understanding plasma catalysis through modelling and simulation — a review, J. Phys. D Appl. Phys. 47 (2014), 224010.
[60] T. Chang, J. Lu, Z. Shen, Y. Huang, D. Lu, X. Wang, et al., Simulation and optimization of the post plasma-catalytic system for toluene degradation by a hybrid ANN and NSGA-II method, Appl. Catal. B Environ. 244 (2019) 107–119.